



Mathematical analysis of mixed convective stagnation point flow over extendable porous riga plate with aggregation and joule heating effects

Hakeem A. Otman^a, Zafar Mahmood^{b,*}, Umar Khan^b, Sayed M. Eldin^c, Bandar M. Fadhl^d, Basim M. Makhdom^d

^a Department of Mathematics, AL-Qunfudhah University College, Umm Al-Qura University, Saudi Arabia

^b Department of Mathematics and Statistics, Hazara University, Mansehra, Pakistan

^c Center of Research, Faculty of Engineering, Future University in Egypt New Cairo 11835, Egypt

^d Mechanical Engineering Department, College of Engineering and Islamic Architecture, Umm Al-Qura University, P. O. Box 5555, Makkah 21955, Saudi Arabia

ARTICLE INFO

Keywords:

Mixed convection
Nanoparticles aggregation
Riga plate
Stagnation point flow
Porous media
Joule heating
Heat source

ABSTRACT

It is still not quite apparent how suspended nanoparticles improve heat transmission. Multiple investigations have demonstrated that the aggregation of nanoparticles is a critical step in improving the thermal conductivity of nanofluids. However, the thermal conductivity of the nanofluid would be greatly affected by the fractal dimension of the nanoparticle aggregation. The purpose of this research is to learn how nanoparticle aggregation, joule heating, and a heat source affect the behavior of an ethylene glycol-based nanofluid as it flows over a permeable, heated, stretched vertical Riga plate and through a porous medium. Numerical solutions to the present mathematical model were obtained using Mathematica's Runge-Kutta (RK-IV) with shooting technique. In the stagnation point flow next to a permeable, heated, extending Riga plate, heat transfer processes and interrupted flow phenomena are defined and illustrated by diagrams in the proposed mixed convection, joule heating, and suction variables along a boundary surface. Data visualizations showed how different variables affected temperature and velocity distributions, skin friction coefficient, and the local Nusselt number. The rates of heat transmission and skin friction increased when the values of the suction parameters were raised. The temperature profile and the Nusselt number both rose because of the heat source setting. The increase in skin friction caused by changing the nanoparticle volume fraction from $\varphi = 0.0$ to $\varphi = 0.01$ for the without aggregation model was about 7.2% for the case of opposing flow area ($\lambda = -1.0$) and 7.5% for the case of aiding flow region ($\lambda = 1.0$). With the aggregation model, the heat transfer rate decreases by approximately 3.6% for cases with opposing flow regions ($\lambda = -1.0$) and 3.7% for cases with assisting flow regions ($\lambda = 1.0$), depending on the nanoparticle volume fraction and ranging from $\varphi = 0.0$ to $\varphi = 0.01$, respectively. Recent findings were validated by comparing them to previously published findings for the same setting. There was substantial agreement between the two sets finding.

* Corresponding author.

E-mail address: zafarmaths222@gmail.com (Z. Mahmood).

Nomenclature

a	Constant
Bi	Biot number (dimensionless)
B_0	Characteristic magnetic field (constant)
B	Variable magnetic field
C_f	Skin friction coefficient
C_p	Specific heat at constant pressure
D	Fractal index
d	The width of the electrodes and magnets is a dimensionless parameter
Ec	Eckert number parameter
f	Dimensionless stream function
j_0	Current density applied to electrode
Gr	Grashof number
g	Gravitational acceleration
L	Characteristic length
k_a	Aggregated thermal conductivity
k	Thermal conductivity
K	Porosity parameter
S	Heat source parameter
N, S	Polarity of magnets for north and south poles
M_0	Magnetization of magnets
Nu_x	Local Nusselt number
Pr	Prandtl number (dimensionless)
M	Magnetic parameter
p	Width of electrode and magnets
Re_x	Local Reynolds number
Z	EMHD parameter
x, y	Cartesian coordinates
u, v	Velocity components
u_e	Free stream velocity
u_w	Stretching velocity
v_w	Mass suction velocity
T_f	Convective temperature
T	Temperature of nanofluid
T_∞	Ambient temperature
ε	Mass suction parameter
γ	Stretching parameter
λ	Mixed convection parameter
φ	Nanoparticles volume fraction
φ_a	Aggregated nanoparticles volume fraction
φ_m	Maximum volume fraction of nanoparticles
r_a, r_p	Radii of aggregated nanoparticles
μ	Dynamic viscosity
ρ	Density
σ	Electrical conductivity
ν	Kinematic viscosity
θ	Dimensionless temperature profile
η	Similarity variable
$[\eta]$	Einstein coefficients
(ρC_p)	Heat capacity
$(\rho \beta_T)$	Thermal expansion

Subscripts

f	Base fluid
nf	nanofluid

1. Introduction

Convective heat transfer is the procedure that occurs when fluid movement moves heat from one site to another. This process may take place in a variety of different environments. A fluid motion that is caused by another factor is referred to as “forced convection,” and the phrase “forced convection” is used to characterize this phenomenon. Free convection is yet another kind of convection is an instance whereby buoyancy forces alone are responsible for producing fluid motion due to density differences. A mixed convection mechanism is produced whenever both natural and forced convection mechanisms are working in conjunction with one another. Because of the widespread use of mixed convection flow in industrial settings, researchers have taken a significant amount of interest in the topic of this kind of flow. Mixed convective flow is used in a variety of applications, some of which are heat exchangers, meteorological barrier zone fluctuations, regenerative and nuclear enthusiasts, and occurrences [1]. Ramachandran and colleagues [2] are credited with the seminal work that was done in the field of computational modeling of mixed convection stagnation point flow across vertical flat surfaces. They made improvements to the work that had been done by Merkin [3], who had discovered a non-unique solution inside a certain assortment of mixed convection.

The fact that ordinary heat transfer fluids have poor thermal conductivity is the primary obstacle to improving the performance of several engineering applications. The reason for this is that conventional heat transfer fluids have always been considered the gold standard [4]. The insertion of solid nanoparticles with high thermal conductivities into the fluids (base fluids) is such a cutting-edge method for increasing the thermal conductivities of such liquids. These nanoparticles may range in size from 1 to 100 nm. Compared to base fluids, nanofluids exhibit greatly improved thermal conductivity and are hence referred to as intelligent heat transfer fluids. Choi [5] made the endeavor to enunciate a new notion of nanofluid, and it is noteworthy to bring to audience attention that numerous references on nanofluids have been identified in Refs. [6–13]. In light of this, a comprehensive analysis of the formulation, and convective transport operations of nanofluids, as well as the mathematical and empirical measurements of thermal conductivity, has been presented [14,15].

Titanium dioxide is an essential component that plays an important role in our day-to-day lives. It is investigated in the field of metallic oxide surface research as crystalline oxides due to the fact that it can function as a photocatalyst and has a very high level of efficiency for the breakdown of ethylene glycol [16]. Because of its capacity to impart whiteness as well as blackness to a variety of objects, such as paintings, papers, and cosmetic products, titanium dioxide powders may be used for a wide variety of purposes. Titanium dioxide has attracted a great deal of interest as a possible candidate for use as a photocatalyst due to the fact that, in comparison to those of other photocatalysts, it has desirable qualities such as high compound strength and a low cost [17,18]. Numerous researchers suggested titanium dioxide, in the form of very small particles, as a potential treatment for serious forms of cancer as well as many other aspects of human existence [19]. Fujishima et al. [20] supplied particular further information on the remarkable titanium dioxide photocatalyst substance for the purpose of atmospheric cleaning.

Aggregates are a term used to describe the ways in which particles or molecules come together to create extended structures. Heterogeneous technological and scientific research places a large emphasis on the aggregation mechanism, which is a process that cannot be reversed. The concepts of aggregation and agglomeration, on the other hand, are not quite the same. The process of assembling chemicals in an arrangement with strong bonding is referred to as aggregation. On the other hand, the process of assembling molecules in a pattern that is only weakly attached and may be disrupted by mechanical force is referred to as agglomeration. Using fractal geometry, one may determine the nature of this aggregation structure. There is a lot of controversy surrounding the idea of increasing nanofluids' thermal conductivity. Recent research indicates that the aggregation of nanocomposite particles plays a significant role in the thermal performance of nanofluids. When compared to Brownian particle motion, Keblinski et al. [21] proposed that major upgrade factors include the size of particles, nanoparticle aggregation, and the liquid-molecule interface. Wang et al. [22] provided evidence that aggregation kinematics may provide thermal conductivity that is both efficient and effective. Fractal theory is capable of providing an accurate description of nanoparticles and their aggregation, according to research by Cai and colleagues [23]. Recently published evidence can be found of several efforts made in this general area; see Refs. [24–26].

As can be seen in Fig. 1, an electromagnetic actuator, often known as a Riga plate, consists of alternating electrodes and permanent magnets that are installed on a flat surface. This breakthrough system for controlling flow, which Gailitis and Lielausis [27] developed, has the ability to produce the Lorentz force. When trying to regulate the flow of an electrically conducting fluid, in addition to the traditional techniques of flow control (such as suction, blowing, and wall motion), one may also make use of electromagnetic body forces. The Riga plate has the potential to cause the wall-parallel Lorentz force to be exerted on the boundary layer. The flow of nanofluids via a Riga plate has beneficial uses in the disciplines of mechanical engineering, chemical technology, architecture, and the biology field [28]. These fields all benefit from the use of nanofluids. In addition to being an essential component for the flow through a Riga plate, the Grinberg term is the factor that is responsible for the generation of the electromagnetic characteristic known as the modified Hartmann number [29]. This factor in the boundary layer momentum equation is decoupled from the flow and decreases at an exponential rate in the direction that is perpendicular to the plate [30]. It was observed that the fluid velocity in the flow that was opposite to the one being opposed decreased. This was because the opposite Lorentz force increased the viscosity of the fluid. The mixed convection nanofluid flow across a Riga plate was then investigated by other researchers (see Refs. [30,31]). The study on the flow over a mixed convective shrinking sheet is a novel sort of shrinking sheet flow, that is basically a backward flow, which was explored by Goldstein [32], and it reveals physical phenomena that are significantly unique from those of the stretched Riga plate. Mishra and Kumar [33] investigated the stimulus that viscous dissipation and heat production or absorption have on an Ag-water nanofluid as it passes over a vertical Riga plate while being subjected to the force of suction.

Because of its considerable significance for biomechanical and architectural processes, the study of flows at the stagnation point has attracted the attention of a great many researchers and experts. In the first study of this kind, Hiemenz [34] used a similarity approach

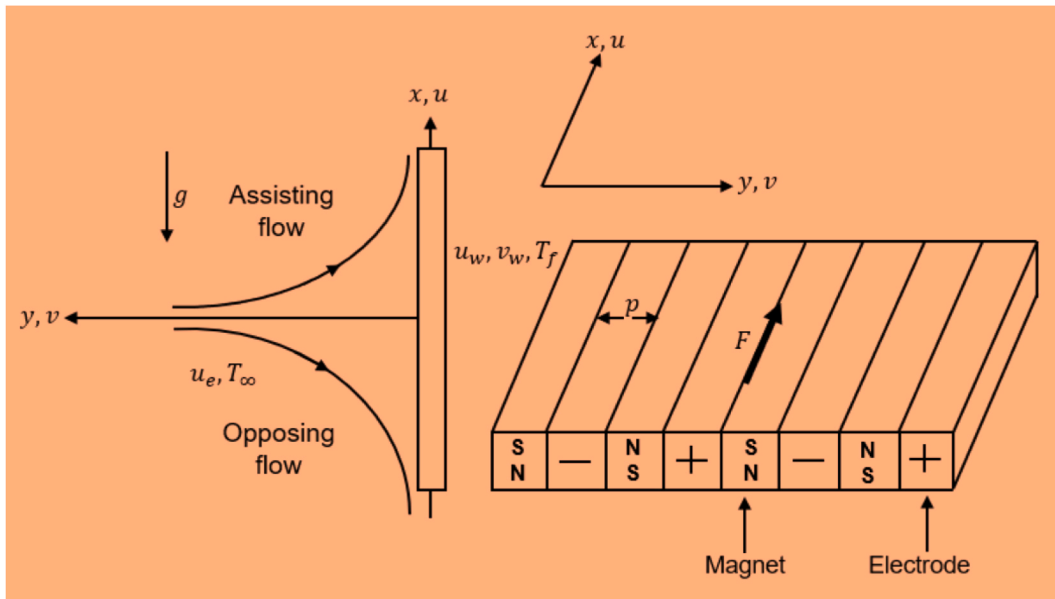


Fig. 1. A graphic depiction of the flow issue is shown.

to reduce the Navier-Stokes equations to non-linear ordinary differential equations in order to examine the 2D stagnation-point flow through a stationary semi-infinite wall. This issue was expanded by Homann [35] to include the axisymmetric stagnation point flow scenario. Wang [36] looked at the axisymmetric as well as the two-dimensional stagnation point flow in a viscous fluid that was moving toward a diminishing sheet.

A substance that has passageways that have been filled with fluid and that moves in either vapor or fluid forms may be described as having the characteristics of a porous medium. The variations in the cavernous and molecular spaces serve to differentiate between inter crystalline porosity and intergranular porosity. As a direct consequence of this, the capability of porous media to facilitate computing applications and research in academia has gained a significant amount of attention. The solid matrix, the structure of the pores, and the amount of porosity in the medium are the primary factors that determine the properties of the medium, including its permeability, thermal conductivity, and heat capacitance. Heat analysis and the design of thermal transfer and exchange devices are finding growing appeal in the use of porous media and transfer media. The process of heat transfer in a fluid is enhanced by the sinuous structure of the medium as it moves through porous media because the fluid encounters the medium's large surface area as it travels through the porous media. In addition, porous media may be exploited to either heat or cool fluids, as well as improve the thermal conductivity of the fluid. Ahmad and Pop [37] investigated the influence that suction had on the buoyancy effects caused by nanofluids implanted in porous medium on a flat vertical plate and found double solutions as a result of their findings. Sheikholeslami et al. [38] conducted an investigation into the effect that a magnetic field has on the flow of fluid that contains nanofluid that is implanted in a source of porous media. They investigated nanofluids in porous media via the cavity using Darcy models and the KKL technique, respectively. Bakar et al. [39] studied the behavior of mixed convective radiative flow when it was directed via a cylinder that contained nanofluid that was generated in a porous media source.

In industrial processes, heat sources and sinks are very important components since the power rating is dependent, to some extent, on the various elements of heat management that govern heat transmission. A great number of investigations have been performed in order to acquire a more in-depth comprehension of the ways in which heat sources and sinks impact the flow of nanofluid boundary layers and the transmission of heat from a variety of points of view. According to Ref. [40], a numerical study was conducted on the mixed convection flow of nanofluid down a vertical plate that included a heat source and a heat sink. In addition [41], explored the combined effects of internal heat production and absorption, thermal radiation, and suction and injection on the mixed convection stagnation point flow of nanofluids in a porous medium over a stretching and shrinking sheet.

To put things another way, a deeper inspection of the works that have been published on the subjects reveals several gaps and discrepancies in the information that they provide. As a result of the knowledge gap that was mentioned earlier, the main aim of this investigation is to examine the nanofluid flow to a vertically permeable heated stretching Riga plate in a porous substrate with the aggregation consequences of nanoparticles, a heat source, joule heating, suction, and mixed convection stagnation point flow, as no prior research has considered this combination of phenomena. We will use a model with and without aggregation to investigate the effect that nanoparticle aggregation has on the mixed convection stagnation point flow via a permeable, heated stretched sheet toward a vertical Riga plate in porous media. This will be accomplished by comparing the results of the model with and without aggregation (see Refs. [24–26]). According to our point of view, the problem is very new and ground-breaking in comparison to the fact that there are no other publications of a similar kind recorded in the literature at this level. The results of the analysis are presented in the form of graphs and tables. In this piece of research, a wide range of characteristics associated with aggregation effects were explored, such as

mixed convection, the volume fraction of solid nanoparticles, the Biot number, the Eckert number, suction, the source of heat, stretching, and the permeability of porous media, the source of heat, stretching, and the permeability of porous media.

2. Mathematical formulation

It is assumed that the $TiO_2/C_2H_6O_2$ nanofluid is flowing toward a permeable, vertically heated porous Riga plate at a stagnation point, with a velocity $u_e(x) = ax/L$, where $a > 0$ (constant) and L is the characteristic length of the Riga plate. Magnets and electrodes make up the Riga plate, which is seen in Fig. 1. The polarity of the magnet is denoted by the letters N and S , which stand for north and south, respectively. The motion (which may assist or oppose) of the Lorentz force is affected by the direction of axial x , which can either be positive or negative. An assumption of changeable wall temperature is established in the existence of mixed convection, nanoparticle aggregation, joule heating, porous media, heat source, and convective phenomena. This assumption is made in such a way that the plate's surface convective temperature is T_f , where T_∞ is the constant far-field temperature.

With these presumptions in place, this leads to the following results for the coupled boundary layer and energy equations, complete with boundary conditions (see Refs. [39,42]):

$$\frac{\partial u}{\partial x} + \frac{\partial v}{\partial y} = 0, \tag{1}$$

$$u \frac{\partial u}{\partial x} + v \frac{\partial u}{\partial y} = u_e \frac{\partial u_e}{\partial x} + \frac{\mu_{nf}}{\rho_{nf}} \frac{\partial^2 u}{\partial y^2} + \frac{g(\rho\beta_T)_{nf}(T - T_\infty)}{\rho_{nf}} + \frac{\pi j_0 M_0 e^{-\pi y/p}}{8\rho_{nf}} - \frac{\mu_{nf} \mathcal{E}}{\rho_{nf} K_1} (u - u_e), \tag{2}$$

$$u \frac{\partial T}{\partial x} + v \frac{\partial T}{\partial y} = \frac{k_{nf}}{(\rho C_p)_{nf}} \frac{\partial^2 T}{\partial y^2} + \frac{Q}{(\rho C_p)_{nf}} (T - T_\infty) + \frac{\sigma_{nf} B_0^2}{(\rho C_p)_{nf}} (u - u_e)^2. \tag{3}$$

In Fig. 1, (u, v) signify the velocities in the (x, y) directions, correspondingly; T represents the temperature of the fluid; g represents the acceleration due to gravity; p indicates the width of the electrodes and the magnets; j_0 represents the current density that is applied to the electrodes; M_0 represents the magnetization of the magnets; and v_w represents the velocity at which wall mass is transferred through the permeable surface. The velocity at which the wall is being stretched is denoted by the symbol $u_w(x)$. K_1 is the constant that represents the permeability of a porous medium. The coefficient of heat transmission by convection is denoted by h_f .

The following are the boundary conditions that are compatible (see Ref. [42]):

$$u = u_w(x), v = v_w(x), -k_{nf} \frac{\partial T}{\partial y} = h_f (T_f - T) \text{ at } y = 0, \tag{4}$$

$$u \rightarrow u_e(x), T \rightarrow T_\infty, \text{ as } y \rightarrow \infty. \tag{5}$$

The correlations between nanofluids (without aggregation and with aggregation) are shown in Table 1, where the subscripts f and nf represent base fluid and nanofluid, respectively. While the symbol φ denotes the volumetric concentration of nanoparticles without aggregation, the symbol φ_a denotes the volumetric concentration of nanoparticles with aggregation. Table 2 lays out the ethylene glycol's and the nanoparticles' thermophysical characteristics for review. The aggregation behavior of the nanoparticles is taken into consideration while selecting the thermophysical characteristics of the nanoparticles. In the absence of aggregation, the effective viscosity and thermal conductivity are computed by using the Brinkman and Maxwell models, respectively. The thermophysical properties of the NP are fine-tuned to account for its tendency to aggregate. As can be seen in Table 1, the use of nanoliquids comes with several distinct benefits.

Table 1
Correlation properties of the nanofluid for aggregation and non-aggregation models (see Refs. [24–26]).

Effective Property	Without Aggregation	With Aggregation
Density	$\frac{\rho_{nf}}{\rho_f} = (1 - \varphi) + \varphi \frac{\rho_s}{\rho_f}$	$\frac{\rho_{nf}}{\rho_f} = (1 - \varphi_a) + \varphi_a \frac{\rho_s}{\rho_f}$
Dynamic Viscosity	$\frac{\mu_{nf}}{\mu_f} = \frac{1}{(1 - \varphi)^{2.5}}$	$\frac{\mu_{nf}}{\mu_f} = \left(1 - \frac{\varphi_a}{\varphi_m}\right)^{[1]\eta\varphi_m}$
Specific Heat Capacity	$\frac{(\rho C_p)_{nf}}{(\rho C_p)_f} = (1 - \varphi) + \varphi \frac{(\rho C_p)_s}{(\rho C_p)_f}$	$\frac{(\rho C_p)_{nf}}{(\rho C_p)_f} = (1 - \varphi_a) + \varphi_a \frac{(\rho C_p)_s}{(\rho C_p)_f}$
Thermal Conductivity	$\frac{k_{nf}}{k_f} = \frac{(k_s + 2k_f) - 2\varphi(k_f - k_s)}{(k_s + 2k_f) + \varphi(k_f - k_s)}$	$\frac{k_{nf}}{k_f} = \frac{(k_a + 2k_f) - 2\varphi_a(k_f - k_a)}{(k_a + 2k_f) + \varphi_a(k_f - k_a)}$
Thermal Expansion	$(\rho\beta_T)_{nf} = (1 - \varphi)(\rho\beta_T)_f + \varphi(\rho\beta_T)_s$	$(\rho\beta_T)_{nf} = (1 - \varphi_a)(\rho\beta_T)_f + \varphi_a(\rho\beta_T)_s$
Electrical conductivity	$\frac{\sigma_{nf}}{\sigma_f} = 1 + \frac{3\left(\frac{\sigma_{nf}}{\sigma_f} - 1\right)\varphi}{\left(\frac{\sigma_{nf}}{\sigma_f} + 2\right) - \left(\frac{\sigma_{nf}}{\sigma_f} - 1\right)\varphi}$	$\frac{\sigma_{nf}}{\sigma_f} = 1 + \frac{3\left(\frac{\sigma_{nf}}{\sigma_f} - 1\right)\varphi_a}{\left(\frac{\sigma_{nf}}{\sigma_f} + 2\right) - \left(\frac{\sigma_{nf}}{\sigma_f} - 1\right)\varphi_a}$

Table 2
 Numerous thermo-physical characteristics of titania, with ethylene glycol serving as the basis fluid (see Ref. [24]).

Properties	TiO ₂	C ₂ H ₆ O ₂
ρ (kg/m ³)	4250	1114
C _p (J/kgK)	686.2	2415
k (W/mK)	8.9538	0.252
β _T (K ⁻¹)	0.9 × 10 ⁻⁵	57 × 10 ⁻⁵

For the Krieger-Dougherty model to be able to compensate for the occurrence of nanoparticle aggregation, it was changed in the way that is outlined in Table 1.

It is represented by the symbol φ_a, and indicates the aggregate volume friction divided by the maximum total packing fraction. This value is derived from aggregate volume friction. The following is the formula that may be used to explain it:

$$\left(\varphi_a = \varphi \left(\frac{r_a}{r_p} \right)^{3-D} \right), \tag{6}$$

It is compatible with the experimental results of TiO₂ – C₂H₆O₂ nanoliquids with the following characteristics when spherical and diffusion-limited aggregation are both considered:

D = 1.8, r_a/r_p = 3.34, φ_m = 0.605 and [η] = 2.5 (see Refs. [24–26]). The Brugman model and the Maxwell model were combined to form the aggregation model of thermal conductivity, which was later revised. To regulate the thermal conductivity of the aggregate, which is represented by the symbol (k_a), calculate it with the help of the following formula (see Refs. [24–26]):

$$\frac{k_a}{k_f} = \frac{1}{4} \left\{ (3\varphi_m - 1) \frac{k_s}{k_f} + (3(1 - \varphi_m) - 1) + \left[\left((3\varphi_m - 1) \frac{k_s}{k_f} + (3(1 - \varphi_m) - 1) \right)^2 + 8 \frac{k_s}{k_f} \right]^{\frac{1}{2}} \right\}. \tag{7}$$

Here, φ_{in} = (r_a/r_p)^{D-3}. Since the similarity transformation satisfied the requirements of the continuity equation (1), the following equation (8) was satisfied as a result (see Refs. [1,42]).

$$u = \frac{ax}{L} f'(\eta), v = -\sqrt{\frac{aw_f}{L}} f(\eta), \theta(\eta) = \frac{T - T_\infty}{T_f - T_\infty}, \eta = \sqrt{\frac{a}{\nu_f L}} y. \tag{8}$$

In this framework, prime signifies difference with respect to η. While $\tilde{v}_w = -\sqrt{\frac{aw_f}{L}} \varepsilon$ and $K_1(x) = \frac{\nu_f \varepsilon L}{K\alpha}$. The following ordinary differential equations may be produced when (1), (2), (3), (4), and (5) are incorporated in the steady-state equations:

$$f'' + \frac{\rho_{nf}/\rho_f}{\mu_{nf}/\mu_f} \left[ff' - f'^2 + 1 + \left(\frac{(\rho\beta_T)_{nf}/(\rho\beta_T)_f}{\rho_{nf}/\rho_f} \right) \lambda \theta + \left(\frac{Z}{\rho_{nf}/\rho_f} \right) e^{-d\eta} - K(f' - 1) \right] = 0, \tag{9}$$

$$\frac{1}{Pr} \frac{k_{nf}/k_f}{(\rho C_p)_{nf}/(\rho C_p)_f} \theta' + f\theta' - f'\theta + S\theta + \frac{1}{(\rho C_p)_{nf}/(\rho C_p)_f} [\sigma_{nf}/\sigma_f Mec(1 - f')^2] = 0, (10) f(\eta) = \varepsilon, f'(\eta) = \gamma, -\frac{k_{nf}}{k_f} \theta'(\eta) = Bi(1 - \theta(\eta)) \text{ at } \eta = 0 \tag{11}$$

$$f'(\eta) \rightarrow 1, \theta(\eta) \rightarrow 0 \text{ as } \eta \rightarrow \infty. \tag{12}$$

Here, $Z = \pi j_0 M_0 / 8a^2 \rho_f$ denotes EMHD parameter, When the EMHD parameter Z is greater than zero, it designates that the Lorentz force is acting in the direction of the positive x– axis, while Z is less than zero and has the opposite effect. The mixed convection parameter $\lambda = Gr/Re_x^2$, where $Gr = g(\beta_T)_f(T_w(x) - T_\infty)x^3 / \nu_f^2$ stands for the Grashof number and $Re_x = xu_e(x)/\nu_f$ stands for Reynolds number. The buoyancy flow that is helping is shown by λ > 0, the force convective flow is represented by λ = 0, and λ < 0 denotes the opposing buoyancy flow. $d = \frac{\pi}{p} \sqrt{\frac{\nu_f}{a}}$ is a dimensionless parameter that represents the width of the electrodes and the magnets. $Pr = (C_p \mu)_f / k_f$ signifies the Prandtl number, $\varepsilon > 0$ is the symbol for the suction parameter. $K = \frac{\nu_f \varepsilon}{\alpha k_0}$ denotes the porosity parameter. The $\gamma = \frac{b}{a}$ is said to stretch or shrink the surface, when γ > 0 signifies the stretching surface. $Ec = \frac{a^2}{(C_p)_f (T_f - T_\infty) L^2}$ is Eckert number, $M = \left(\frac{a}{\rho} \right) \frac{B_0^2}{f}$ represent the magnetic (MHD) parameter, $Bi = \frac{h_f}{k_f} \sqrt{\frac{\nu_f}{a}}$ is the biot number and $S = \frac{LQ}{(\rho C_p)_{nf}}$ is the source parameter.

3. Physical quantities of interest

Each of the local Nusselt number Nu_x and the coefficients of skin friction C_f has an equation to represent it.

$$C_f = \frac{\tau_w}{\rho_f u_e^2} \text{ and } Nu_x = \frac{xq_w}{k_f(T_f(x) - T_\infty)} \tag{13}$$

where $\tau_w = \mu_{nf} \left(\frac{\partial u}{\partial y}\right)_{y=0}$ designates the surface shear stress while $q_w = -k_{nf} \left(\frac{\partial T}{\partial y}\right)_{y=0}$ is the surface heat flux. When the similarity transformation from Equation (8) is applied to Equation (13), together with a representation of shear stress and surface heat flux, the reduced skin friction coefficient and local Nusselt number (heat transfer rate) of the nanofluid are found to be.

$$Re_x^{1/2} C_f = \frac{\mu_{nf}}{\mu_f} f''(0), Re_x^{-1/2} Nu_x = - \left(\frac{k_{nf}}{k_f}\right) \theta'(0). \tag{14}$$

4. Numerical procedure and code validation for solution

An attempt is made to resolve the governing problem by using the Runge-Kutta fourth-order numerical integrating approach in conjunction with a shooting procedure. In order to put this method into action, the governing issue will first and foremost be broken down into a set of concurrent equations of the first order of differential order. This will allow the problem to be more easily analyzed and solved. Let us suppose:

$$m_1 = f, m_2 = f', m_3 = f'', m_4 = f''', n_1 = \theta, n_2 = \theta', \tag{15}$$

applying equation (15)

$$m_1' = f', m_2' = f'', m_3' = f''', m_4' = f^{(4)}, n_1' = \theta', n_2' = \theta'', \tag{16}$$

here is a rundown of the outcomes we obtained using equations (15) and (16).

$$m_1' = m_2, m_2' = m_3, m_3' = m_4, n_1' = n_2, n_2' = n_3, \tag{17}$$

by writing equations (15)–(17) as bellows, we get the values of f'' and θ'' .

$$m_4 = - \frac{\rho_{nf}}{\mu_f} \left[m_1 m_3 - m_2^2 + 1 + \left(\frac{\rho\beta_T}{\rho_{nf}}\right)_{nf} / \left(\frac{\rho\beta_T}{\rho_f}\right)_f \lambda n_1 + \left(\frac{Z}{\rho_{nf}/\rho_f}\right) e^{-d\eta} - K(m_2 - 1) \right], \tag{18}$$

$$n_3 = - Pr \frac{(\rho C_p)_{nf} / (\rho C_p)_f}{k_{nf} / k_f} \left[\left(m_1 n_2 - m_2 n_1 + Sn_1 + \frac{1}{(\rho C_p)_{nf} / (\rho C_p)_f} [\sigma_{nf} / \sigma_f M E c (1 - m_2)^2] \right) \right] \tag{19}$$

$$m_1 = \varepsilon, m_2 = \gamma, - \frac{k_{nf}}{k_f} n_2 = Bi(1 - n_1), m_3 \rightarrow 1, n_2 \rightarrow 0. \tag{20}$$

The missing starting conditions are denoted by the symbols m_2, n_1 and m_3 . Iteratively using the Newton-Raphson approach allows for the estimation of appropriate values for beginning circumstances for which values are unknown. After the missing conditions have been satisfied, we will proceed to apply the aforementioned numerical strategy. In order to guarantee asymptotic convergence, the choice of η_∞ ranges from 3 to 10, and the error introduced by simulation is 10^{-5} with step size $\Delta\eta = 0.001$.

The juxtaposition of the models is elaborated upon in Tables 3 and 4, which contrast the $(Re_x^{1/2} C_f)$ and $(Re_x^{-1/2} Nu_x)$ for $Z = K = S = \gamma = d = \lambda = M = Bi = Ec = 0$ (flat plate without EMHD) between the present work and those of Khashi et al. [42]. In addition to the section in which the model is verified, this is new material. While the authors of [42] used the bvp4c solver in MATLAB, we were able to get the job done by employing MATHEMATICA's RK-IV with the shooting technique. Furthermore [42], relied on the Devi and Devi models, whereas we used the aggregation model. As can be observed in Tables 3 and 4, the results reported here accord pretty well with the results presented in Ref. [42]. This can be seen by comparing the two sets of data. The researchers are optimistic that they will be

Table 3
The values of $(Re_x^{1/2} C_f)$ for φ when $\gamma = \varepsilon = \lambda = Bi = K = d = Z = M = Ec = S = 0$ and $Pr = 6.2$ with no occurrences of aggregation.

φ	Present	Researcher of [42]
0.05	1.5539	1.5538
0.10	1.8444	1.8443
0.15	2.2370	2.2369
0.2	2.6226	2.6227

Table 4

The values of $(Re_x^{-1/2}Nu_x)$ for ϕ when $\gamma = \varepsilon = \lambda = Bi = K = d = Z = M = Ec = S = 0$ and $Pr = 6.2$ with no occurrences of aggregation.

ϕ	Present	Researcher of [42]
0.05	1.7759	1.7758
0.10	1.9694	1.9692
0.15	2.1592	2.1593
0.2	2.3493	2.3494

able to successfully apply this strategy and model to their work because of the findings presented here. The whole of the numerical information that is pertinent to the reduced state of a Newtonian fluid may be found in [Tables 3 and 4](#)

5. Results and discussion

In this part, we will explore the graphical data for velocity $f(\eta)$, temperature $\theta(\eta)$, skin friction $Re_x^{1/2}C_f$, and Nusselt number $Re_x^{-1/2}Nu_x$ in [Fig. 2 through 15](#), which collectively provide a full picture of the current state. $TiO_2/C_2H_6O_2$ is studied in terms of (a) aggregation effects on nanoparticles and (b) the lack of aggregation effects. The orientation of the variables is the same in both cases (a and b), even though the numerical values of the parameters are different in the two scenarios. Despite this, it was thought that the Prandtl number was 204, even though comparisons were made with the earlier instance. The estimations of the control parameters have been updated so that they are consistent with the tables and figures. These numbers are chosen in accordance with the far-field boundary criteria (11, 12). In this study, we select the values of nanoparticles volume fraction $0.0 \leq \phi \leq 0.05$. Further variables such as $\lambda \in [-1, 1]$ (mixed convection), $K \in [2, 2.5]$ (porosity), $\varepsilon \in [2, 2.5]$ (suction) and $Z \in [-0.5, 0.5]$ (EMHD), $0.0 \leq Ec \leq 1.0$ (Eckert number), $0.0 \leq Bi \leq 1.0$ (biot number), $\gamma \in [0, 1.0]$ (stretching), $0.0 \leq M \leq 1.0$ (magnetic field), $S \in [0.0, 1.0]$ (heat source) and $d = 0.5$ (width of electrode and magnets parameter fixed in this study) are decided upon in line with the most significant references and solutions that may be discovered in the assisting/opposing flow.

The suction parameter ε in the opposite flow zone ($\lambda = -0.5$) is shown to take on a wide range of values in [Fig. 2 \(A\) and 2 \(B\)](#) for the $f'(\eta)$ and $\theta(\eta)$ profiles of both the no-aggregation and the aggregation models, respectively. This may be seen by looking at [Fig. 2 \(A\)](#), which demonstrates that the quantity of $f'(\eta)$ increased noticeably when the sharp rise-up amount of ε was applied. An increase in ε results in a greater rate of fluid evacuation from the boundary, which in turn causes a larger pressure differential inside the boundary layer. The evidence suggests that this is the situation from a purely physical standpoint. Because of this, there is an upsurge in the $f'(\eta)$ at the boundary, and as a result, there is an elevation in the velocity gradient. The thickness of the momentum barrier layer was able to get thinner as a result of this process, which resulted in an improvement in the shear stress at the wall. In addition, this result is consistent with the data shown in [Fig. 6\(C\)](#), which shows that the amount of skin friction rises as the ε grows. As the suction force increases, not only does the thickness of the thermal boundary layer diminution, but the $\theta(\eta)$ profile does as well, as shown in [Fig. 2\(B\)](#), which shows the relationship between the two variables. If we reduce the thickness of the thermal boundary layer, we will be able to generate greater heat flow. This is because of the way that matter, and energy interact. Because of this event, the performance of the heat transmission was significantly improved. This conclusion is consistent with what happens, and the remark shown in [Fig. 6\(D\)](#), which shows that an upsurge in the Nusselt number occurs in conjunction with an intensification in the suction force. In this scenario, the aggregation model displays more favorable outcomes.

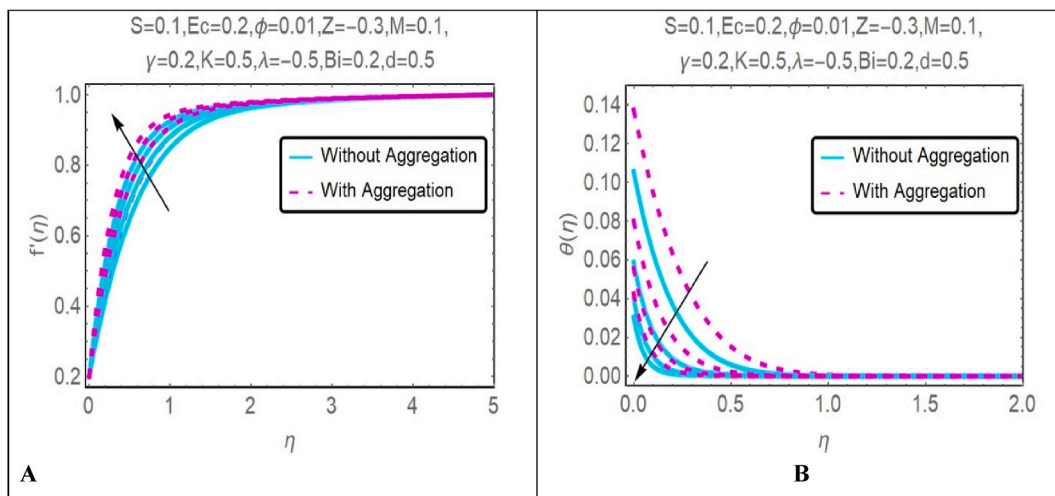


Fig. 2. (A) The impact that different values of suction ($\varepsilon = 2.0, 2.1, 2.2, 2.3$) have on $f'(\eta)$. (B) Changes in $\theta(\eta)$ for $\varepsilon = 2.0, 2.1, 2.2, 2.3$.

Fig. 3(A)–(B), respectively, demonstrate the effect of mixed convection parameters λ against $f'(\eta)$ and $\theta(\eta)$ profiles for $TiO_2/C_2H_6O_2$ nanofluid for both instances with aggregation and without aggregation. It has been shown that the velocity field, $f'(\eta)$, dramatically increases when the value of λ continuously increases from -1 to 1 . This is due to the increased hydrostatic pressure; greater values of λ suggest an elevated hydrostatic pressure if they correspond with a greater flow field. The reason for this is that the flow field is higher. Within the boundary layer domain, the thermal buoyancy factor quantifies the degree to which the thermal buoyancy force has a comparative impact on the viscous hydrodynamic force. As demonstrated in Fig. 3(B), when the quantity of λ continues growing, the $\theta(\eta)$ has been shown to exhibit a tendency toward a lowering temperature.

The rise in Z contributed significantly to the improvement of the velocity profile. The increase in Z was physically related to an enlargement of the electrical field that is accountable to produce the Lorentz force. This field is responsible for the development of the Lorentz force. The boundary layer decreased as a direct consequence of this force, which led to a boost in the $f'(\eta)$ profile (as can be seen in Fig. 4(A)). After that, a further increase in Z led to an overshoot in the $f'(\eta)$ profiles (see Fig. 4(A)), which shows that the $f'(\eta)$ of the $TiO_2/C_2H_6O_2$ nanofluid close to the Riga plate was greater than the free stream velocity when strong Lorentz forces were present. In the meantime, as Z grew, the thermal boundary layer shrank and became more constrained. After that, a further reduction in the $\theta(\eta)$ profile was noticed (see Fig. 4(B) for more information), which corroborated the logic presented in Fig. 8(C) further below.

Fig. 5(A)–(B), respectively, shed light on the effects that ϕ has on the $f'(\eta)$ and $\theta(\eta)$ of the $TiO_2/C_2H_6O_2$ nanofluid without and with aggregation models. When the ϕ is increased from 1% to 4%, the viscosity and thermal conductivity are both improved, which outcomes in a growth in $f'(\eta)$ as well as an increase in $\theta(\eta)$. A nanolayer forms in the fluid around the nanoparticles because of the formation of clusters by the nanoparticles. This nanolayer serves as a momentum and thermal bridge between the particle's motion and

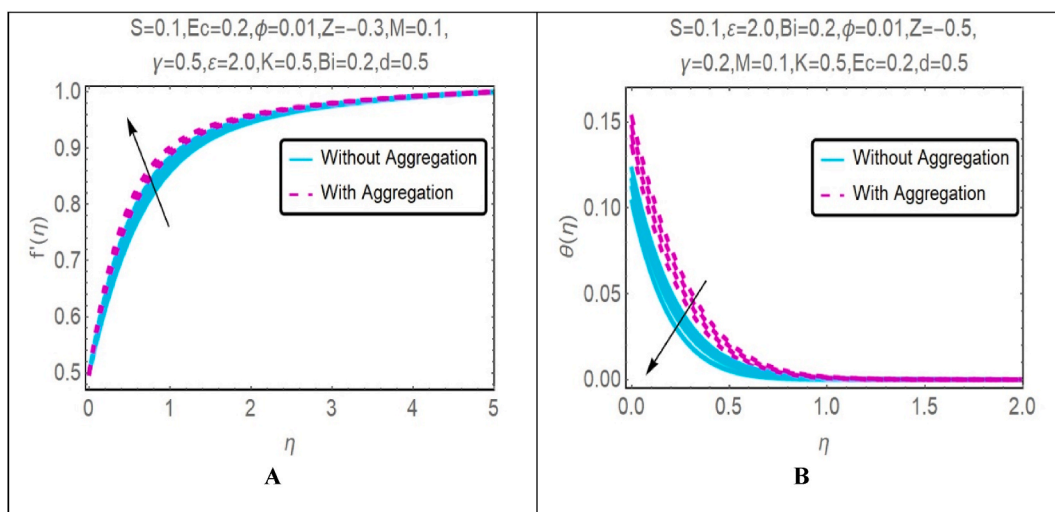


Fig. 3. (A): Significance of $(\lambda = -1.0, -0.5, 0.5, 1.0)$ on $f'(\eta)$. (B): Stimulus of $(\lambda = -1.0, -0.5, 0.5, 1.0)$ on $\theta(\eta)$.

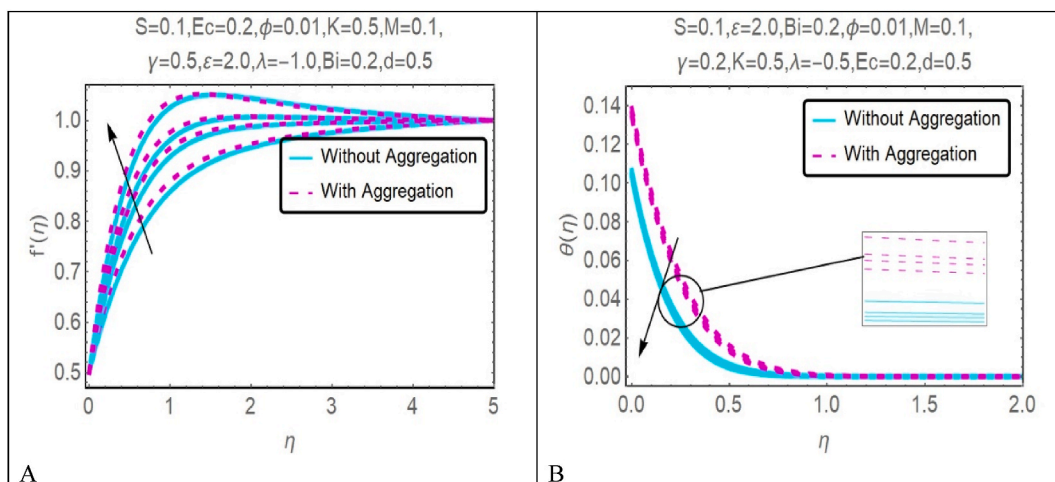


Fig. 4. (A): Significance of $Z = -0.5, -0.1, 0.1, 0.5$ on $f'(\eta)$. (B): Effect of $Z = -0.5, -0.1, 0.1, 0.5$ on $\theta(\eta)$.

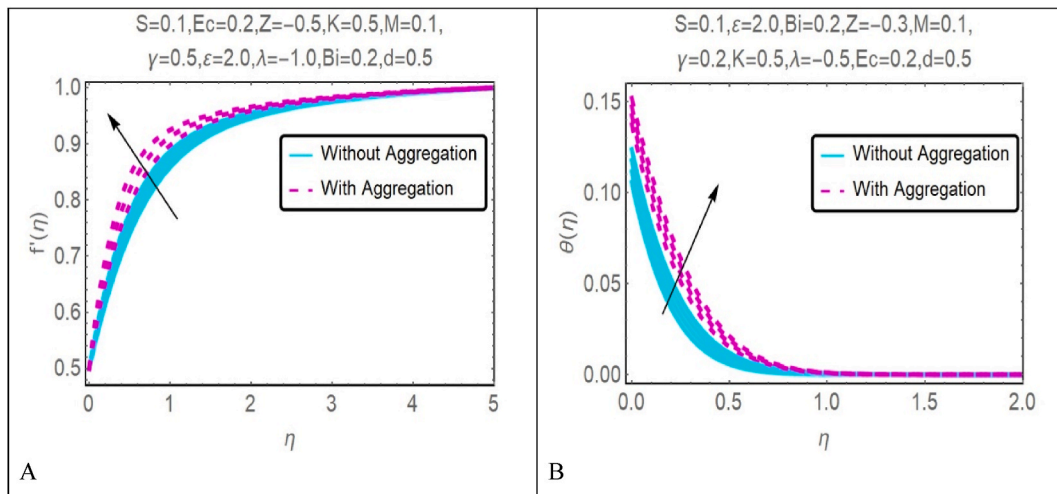


Fig. 5. (A): Significance of $\varphi = 0.01, 0.02, 0.03, 0.04$ on $f'(\eta)$. (B): Stimulus of $\varphi = 0.01, 0.02, 0.03, 0.04$ on $\theta(\eta)$.

the aggregation of nanofluids. The thickness of the nanolayer is an important factor in improving both the viscosity and the thermal conductivity of the material. This nanolayer theaters a noteworthy role in the transmission of heat from the solid to the fluid that is close to it. The presence of nanoparticles in this scenario results in the aggregation process producing temperature and velocity profiles that are more extreme.

Fig. 6(A)–(B), respectively, illustrate the impact of the porosity parameter K on the $f'(\eta)$ and $\theta(\eta)$ profiles of $TiO_2/C_2H_6O_2$ nanofluid with and without aggregation effects. It has been observed that a porous medium with a greater permeability also has a greater porosity value than a medium with a lower permeability. It has been noticed that there is an association between a growth in the porosity factor and a thickening of the boundary layer. This is because differences in permeability produce reductions in heat flow, which in turn cause a boost in the temperature gradient. The buoyant forces pick up speed when the norms close to the Riga plate surface go up, while the negative response may be seen farther away from the surface. According to these figures, a boost in K led to a rise in the $f'(\eta)$ of $TiO_2/C_2H_6O_2$ nanofluid for both the homogeneous model and the aggregation model, but it resulted in a drop in the $\theta(\eta)$ of the $TiO_2/C_2H_6O_2$ nanofluid. As demonstrated in Fig. 6 (A), an increase in K resulted in a narrowing of the diameter of the momentum boundary layer. The thermal boundary layer depth increased in a manner that was comparable to that shown in Fig. 6 (B), which showed rising K values. When compared side-by-side, the graphs illustrating the absence and presence of aggregation revealed that the estimated thickness of momentum and thermal boundary layers was thinner for velocity profiles and thicker for temperature profiles.

Figs. 7 and 8 demonstrate, respectively, the influences of the heat source parameter, S , the biot number, Bi , the Eckert number, Ec and the magnetic parameter, M , on temperature profiles for $TiO_2/C_2H_6O_2$ nanofluid without and with aggregation. This is shown in Fig. 7 (A), which shows how the $\theta(\eta)$ profile changes in accordance with the source parameter S . The temperature profile increases in a

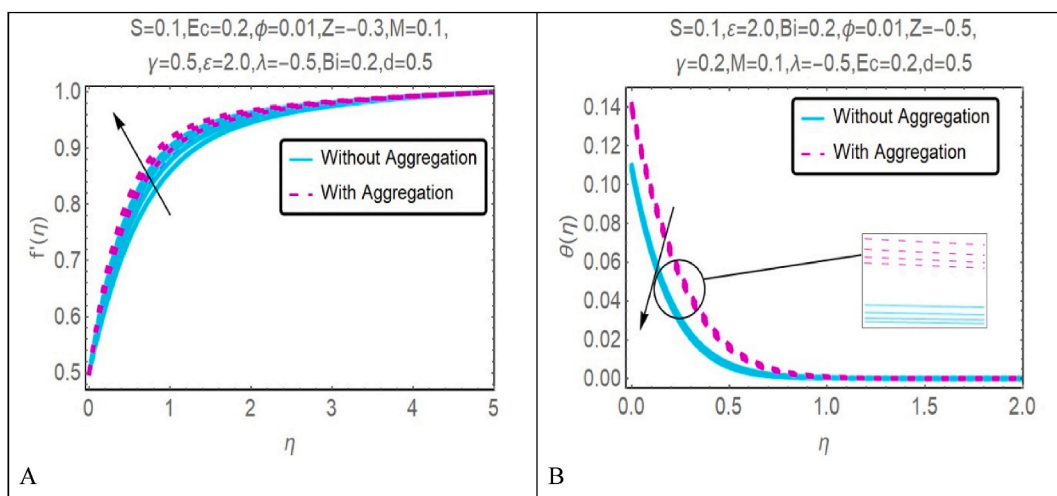


Fig. 6. (A): Significance of $K = 0.5, 1.0, 1.5, 2.0$ on $f'(\eta)$. (B): Impression of $K = 0.5, 1.0, 1.5, 2.0$ on $\theta(\eta)$.

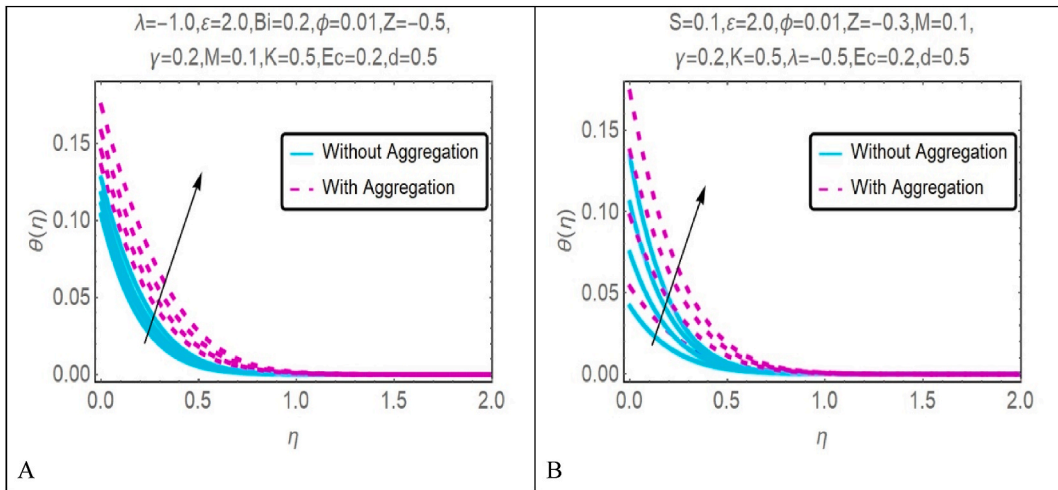


Fig. 7. (A): Significance of $S = 0.2, 0.4, 0.6, 0.8$ on $\theta(\eta)$. (B): Stimulus of $Bi = 0.1, 0.2, 0.3, 0.4$ on $\theta(\eta)$.

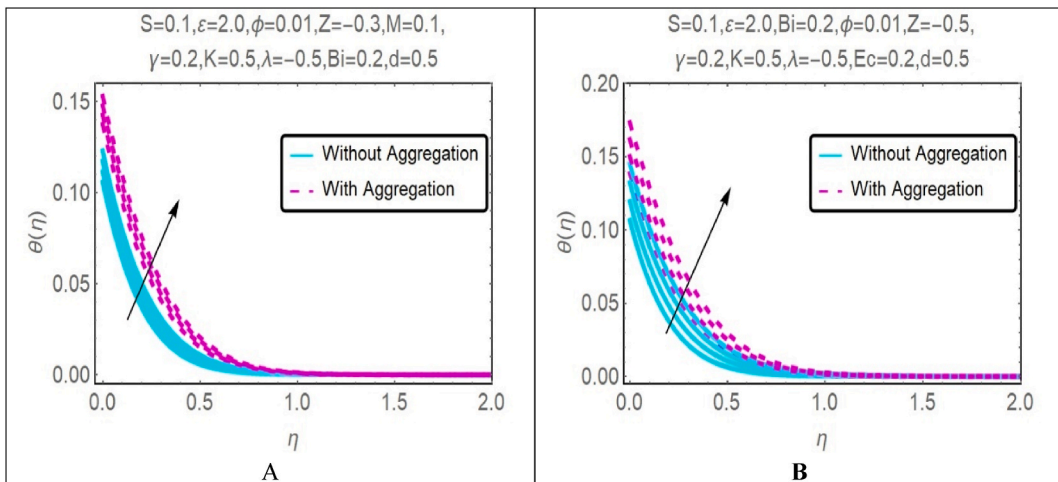


Fig. 8. (A): Impact of $Ec = 0.2, 0.4, 0.6, 0.8$ on $\theta(\eta)$. (B): Influence of $M = 0.1, 0.2, 0.3, 0.4$ on $\theta(\eta)$.

manner that is completely consistent with the source parameter S . Because an increase in the value of the heat source parameter causes a greater amount of energy to be generated at the thermal boundary layer, this can lead to an increase in both the thickness of the thermal layer and the thermal gradient. Following that, the profiles of $\theta(\eta)$ in Fig. 7(B) emphasize the impact of Biot number, Bi , in regions of opposing flow ($\lambda = -0.5$). The importance of Bi may be underlined by referring to Fig. 7(B), which shows that the surge-up Bi value has a significant impact on the temperature profile between $\eta = 0$ and $\eta \rightarrow \infty$. The Biot number is an indicator that determines the connection between the convection that occurs at the surface of a solid and the conduction that occurs inside the solid. As Bi increases, an upward trend in the $\theta(\eta)$ profile can be observed as well. When viewed from a purely physical perspective, a surface's thermal resistance will gradually decrease as the Biot number increases. The rise in convection is responsible for the rise in surface temperature as well as the increased thickness of the thermal boundary layer that has been built up. In addition, the heat flow was decreased, which contributed to the strengthening of the thermal boundary layer. This resulted in a reduction in heat transfer performance as the value of Bi increased.

The behavior of $\theta(\eta)$ is shown in Fig. 8(A) with Ec modified in opposing flow ($\lambda = -1.0$). The rise in temperature may be seen because of the spike-up value of Ec , which is shown in Fig. 8 (A). In a sense that pertains to the physical world, the Eckert number qualities are connected to the Joule heating components that are included in the energy equation. Because of the magnetic resistance that is formed from the Lorentz force in addition to the friction inside the fluid, the mechanical energy that is combined with the electrical energy is converted into heat. Consequently, an increase in Ec will also result in an increase in $\theta(\eta)$, which will cause the thermal boundary layer to become thicker and result in a lower heat flux. This process decreased the concert of heat transfer as Ec grew, and this finding is consistent with the conclusion shown in Fig. 15 (B), in which the $Re_x^{-1/2}Nu_x$ was lowered in conjunction with the quickening of Ec .

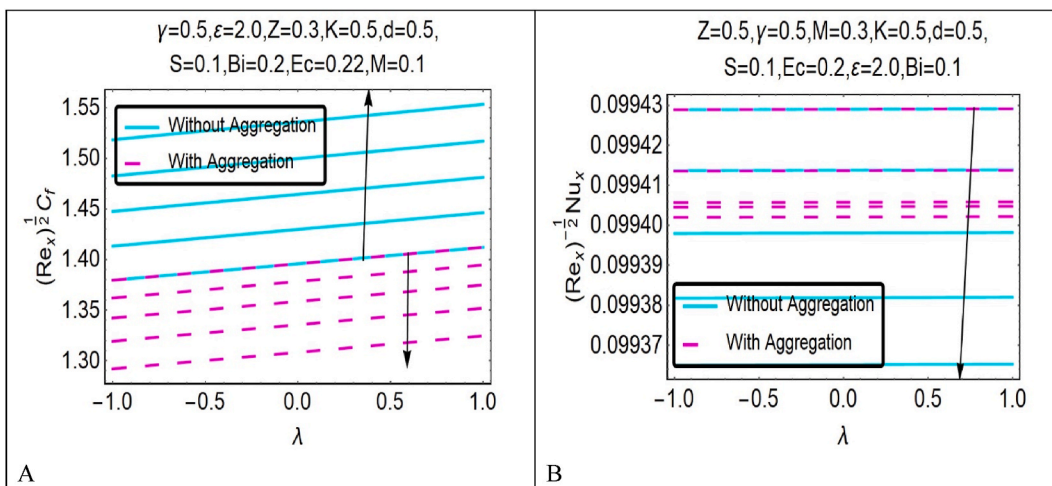


Fig. 9. (A): Variation in $Re_x^{1/2} C_f$ for ϕ against λ . (B): Variation in $Re_x^{-1/2} Nu_x$ for ϕ against λ .

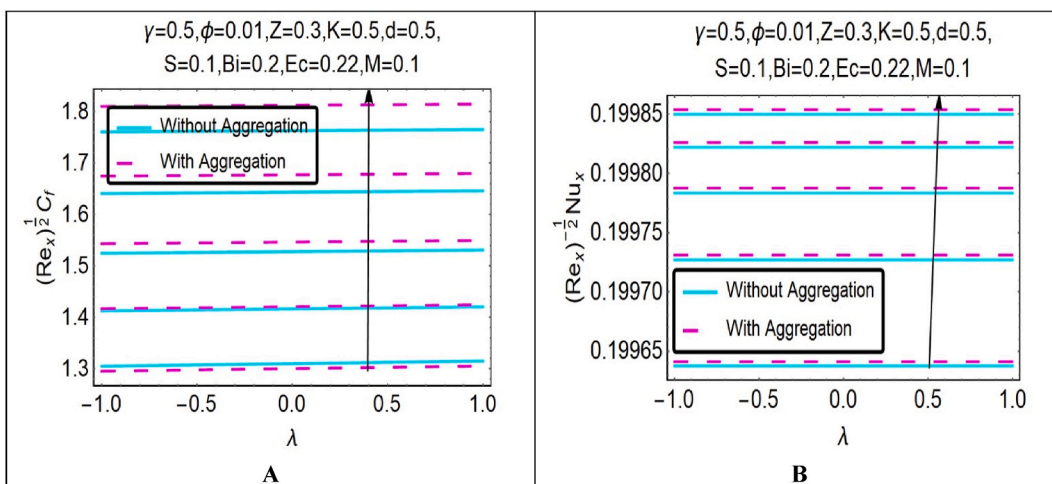


Fig. 10. (A): Change in $Re_x^{1/2} C_f$ for ϵ with λ . (B): Alteration in $Re_x^{-1/2} Nu_x$ for ϵ with λ .

Fig. 8(B) illustrates the patterns of $\theta(\eta)$ because of modifying the magnetic parameter, M , in the zone of opposing flow ($\lambda = -1.0$). These behaviors are shown in the context of the region. As shown in Fig. 8(B), the accumulation of $\theta(\eta)$ in the thermal boundary layer leads to an intensification in the $\theta(\eta)$ profile with a higher value of M . Because of this occurrence, there is an overall rise in the $\theta(\eta)$ profile. Physically speaking, the impact of M , together with the numerous components in this fluid flow issue, such as Joule heating and convective boundary conditions, pump up the quantity of heat energy, which thickens the thermal boundary layer. In other words, the effect of M thickens the thermal boundary layer more. As a result of this, both the heat flux and the heat transfer rate decreased, and evidence of this can be seen in the outcome of Fig. 14(B), which illustrates the value of the $Re_x^{-1/2} Nu_x$ decreasing as M increases. Both factors contributed to the decrease in the heat transfer rate.

The behavior of the physical parameters in relation to the velocity and temperature profiles is shown in Figs. 2–8 for both the “without aggregation” and “with aggregation” instances, respectively. In addition, it has been observed that the velocity and temperature are larger when there is aggregation present as opposed to when there is not. This is the case as compared to the situation in which there is no aggregation present. Asymptotically, when $f(\eta)$ and $\theta(\eta)$ were carried out, all profiles met the far-field boundary criteria (11, 12). When $\eta_\infty = 8$ was carried out, this was the situation that arose.

The differences between the no-aggregation and aggregation models of $TiO_2/C_2H_6O_2$ nanofluid are shown in Fig. 9(A)–(B), which show the dynamics of $Re_x^{1/2} C_f$ and $Re_x^{-1/2} Nu_x$ versus λ with ϕ . As seen in Fig. 9(A), the model without aggregation demonstrates an increasing trend, whereas the model with aggregation effects demonstrates a decreasing trend regarding different amounts of ϕ for both ranges in the assisting ($\lambda > 0$) as well as opposing ($\lambda < 0$) flow regions. According to the results, the existence of aggregated solid nanoparticles could be the principal contributor to the observed variance in $Re_x^{1/2} C_f$ levels. This conclusion was reached after analyzing

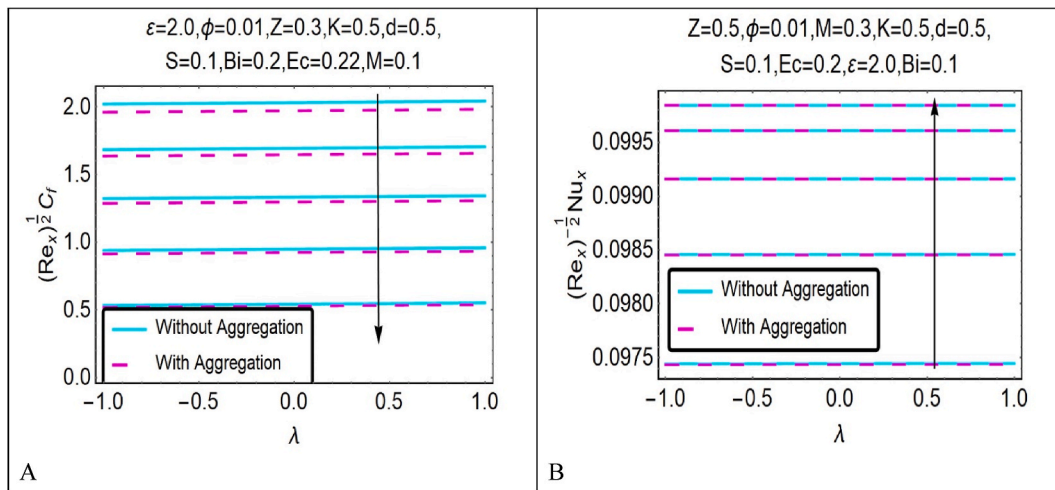


Fig. 11. (A): Change of $Re_x^{1/2} C_f$ for $\gamma = 0.2, 0.4, 0.6, 0.8, 1.0$ versus λ . (B): Change of $Re_x^{-1/2} Nu_x$ for $\gamma = 0.2, 0.4, 0.6, 0.8, 1.0$ against λ .

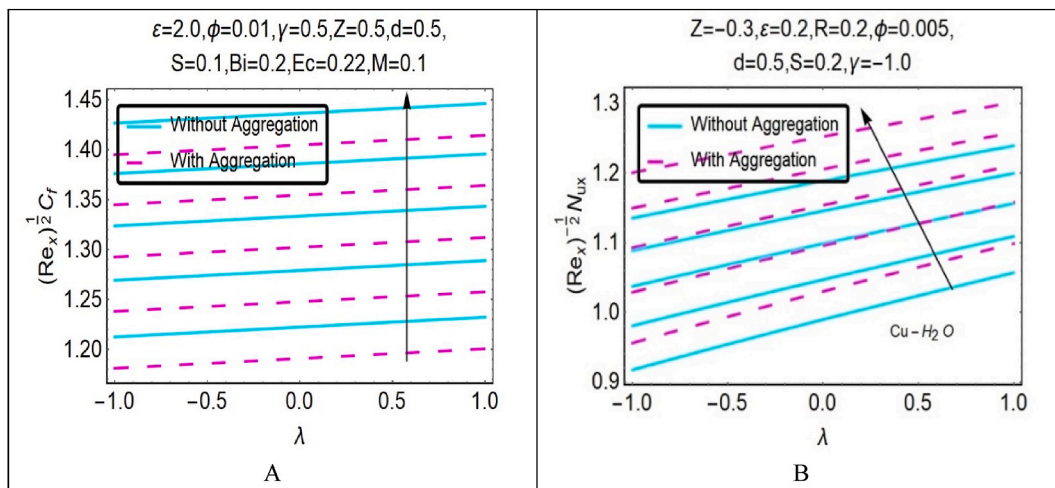


Fig. 12. (A): Variation of $Re_x^{1/2} C_f$ for $K = 0.5, 1.0, 1.5, 2.0, 2.5$ against λ . (B): Variation in $Re_x^{-1/2} Nu_x$ for $K = 0.5, 1.0, 1.5, 2.0, 2.5$ against λ .

the data. The physical performance of the fluid's viscosity was shown to be improved without the aggregation effect becoming a factor at higher values for the nanoparticle volume percent. As a direct consequence of this, the thickness of the momentum boundary layer is reduced, which improves the flow of fluid and raises the surface shear stress. Following that, the graphical findings that were presented in Fig. 9(B) demonstrated that the presence of aggregation increased the rate of heat transfer when contrasted with the absence of aggregation for a greater amount of $Re_x^{-1/2} Nu_x$. This suggests that the presence of aggregation may increase the rate of heat transfer if there is a lower thickness in the thermal boundary layer, which results in a larger heat flow when compared to the absence of aggregation. In addition, this discovery provides support for the hypothesis that an increase in the temperature gradient may result from the presence of additional effects or components that are present in the flow. This shows that having aggregation can put off boundary layer separation as well as enhance the range of solutions when compared to situations in which there is no aggregation present.

Fig. 10(A) and (B) illustrate the distribution of $Re_x^{1/2} C_f$ and $Re_x^{-1/2} Nu_x$ approaching dimensionless λ with varied amounts of ϵ for models with and without aggregation, respectively. It can be observed from what is shown in Fig. 10 (A) that the value of $Re_x^{1/2} C_f$ increased when there was an increase in the amount of ϵ in both the areas that had opposing and aiding flow. Because of the action of the suction at the boundary, the motion of the nanofluid slows down, and the velocity gradient on the surface grows. This has a physical consequence. Therefore, the heated fluid is pulled toward the wall according to the influence of suction, and as a result, a rapid gradient of velocity is produced. This is because the buoyant forces decrease as a result of the substantial change in viscosity. As a result, this event resulted in an increase in the shear stress that was present at the wall as well as an increase in the momentum that was present in the boundary layer. This suggests that the increase in the strength of the suction might potentially postpone the boundary layer or flow separation. The permeable sheet helps to keep the laminar flow going by encasing the molecules that are traveling slowly

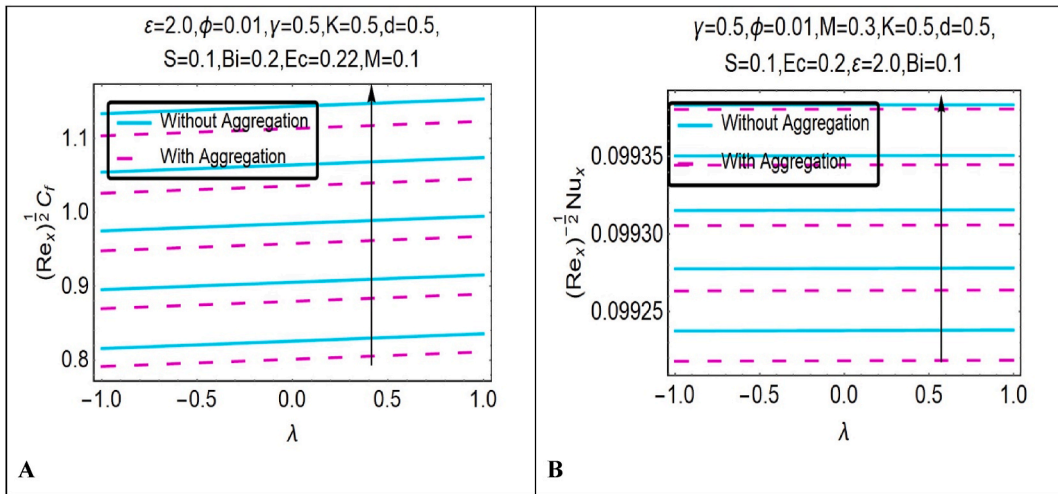


Fig. 13. (A): Change in $Re_x^{-1/2} C_f$ for $Z = 0.5, -0.2, 0.0, 0.2, 0.5$ against λ . (B): Variation in $Re_x^{-1/2} Nu_x$ for $Z = -0.5, -0.2, 0.0, 0.2, 0.5$ against λ .

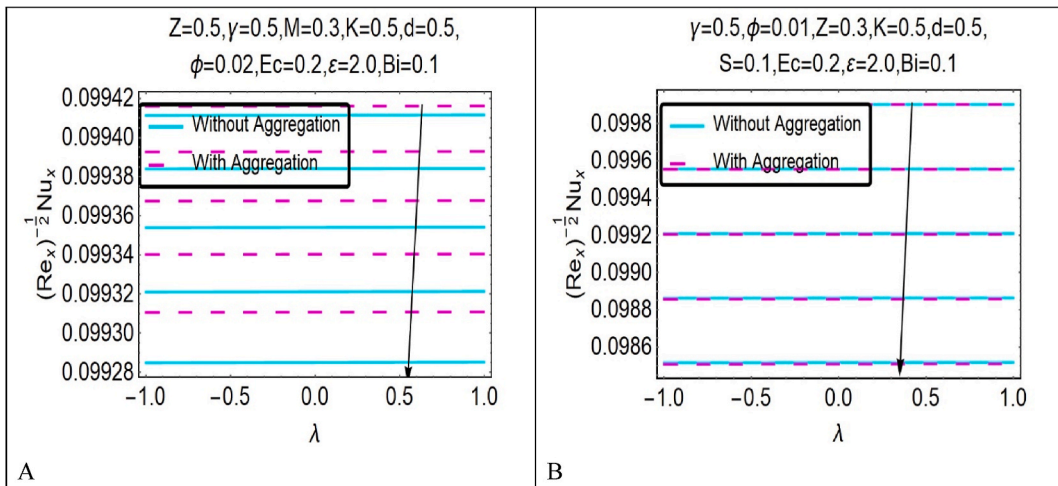


Fig. 14. (A): Variations in $Re_x^{-1/2} Nu_x$ for $S = 0.2, 0.4, 0.6, 0.8, 1.0$ against λ . (B): Influence of $M = 0.2, 0.4, 0.6, 0.8, 1.0$ with λ towards $Re_x^{-1/2} Nu_x$.

in its stretched sheet. This makes it easier to keep the flow laminar. In addition to this, as shown in Fig. 10 (B), the value of the $Re_x^{-1/2} Nu_x$ increases as the suction intensity increases over time. As a result of the function that suction plays in creating fluid motion, which concurrently assists heated particles in migrating closer to the wall, a faster rate of heat transfer is obtained from a purely physical perspective. As the value increases, more ferrofluid particles are able to diffuse through the sheet, which results in an increase in the sheet's permeability. As a result, this phenomenon causes a greater contribution of heat flow while simultaneously reducing the thickness of the thermal barrier layer. As a result, an increase in suction speeds up the pace at which heat is transferred.

Figs. 11 and 12 show, respectively, the implications of the γ and the porosity constraints K against the λ for $(Re_x^{-1/2} C_f)$ and $(Re_x^{-1/2} Nu_x)$. These figures are applicable to both scenarios. Fig. 11(A) shows that, for both aggregation-free and aggregation affected nanofluids, the $(Re_x^{-1/2} C_f)$ have been reduced as a function of the stretching parameter γ in the direction of λ . This happens when the buoyancy force decreases, which ultimately leads to the fluid velocity to increase. This results in a reduction in the wall shear stress, which, in turn, leads to a reduction in the $(Re_x^{-1/2} C_f)$. In Fig. 11 (B), illustrate how the $(Re_x^{-1/2} Nu_x)$ was maximized in relation to the stretching parameter γ towards λ for $TiO_2/C_2H_6O_2$ nanofluid in both cases where aggregation effects were present and where they were absent. When the value of γ is increased, there is a corresponding upsurge in the temperature gradient and a decrease in the thermal boundary layer. $TiO_2/C_2H_6O_2$ nanofluid with aggregation has a graph with a higher $(Re_x^{-1/2} C_f)$ and $(Re_x^{-1/2} Nu_x)$ than $TiO_2/C_2H_6O_2$ nanofluid without aggregation does.

It was discovered, via examination of Fig. 12 (A) and 12 (B), that increased K values led to an increase in the values of $(Re_x^{-1/2} C_f)$ and $(Re_x^{-1/2} Nu_x)$. This discovery suggested that this parameter had a significant influence on the types of solutions that might be discovered. As a direct consequence of this, it was successfully demonstrated that the porous media influenced the partitioning of the

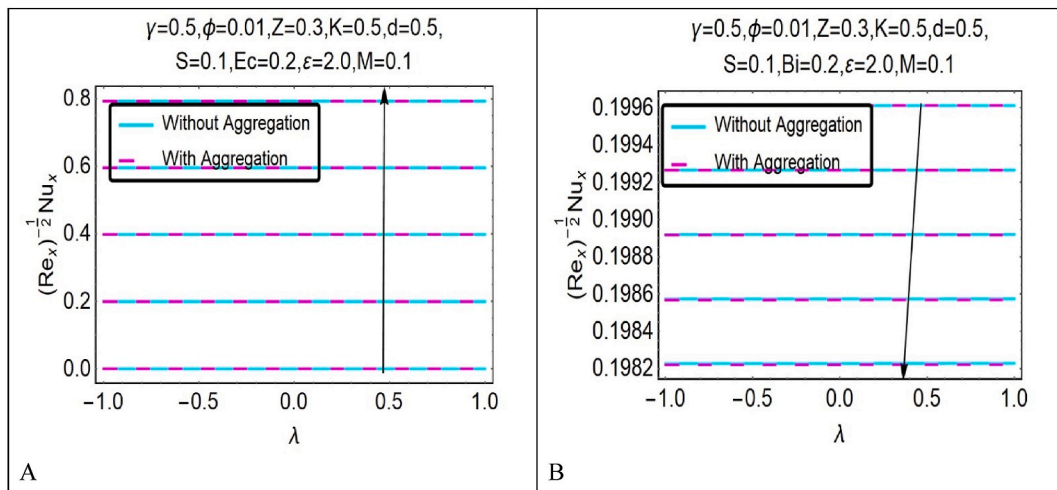


Fig. 15. (A): Influence of $Bi = 0.2, 0.4, 0.6, 0.8, 1.0$ with λ on $Re_x^{-1/2}Nu_x$. (B): Influence of $Ec = 0.2, 0.4, 0.6, 0.8$ with λ on $Re_x^{-1/2}Nu_x$.

nanofluid boundary layer. Fig. 13 (A) and 13 (B) demonstrate that the graph of $(Re_x^{1/2}C_f)$ and $(Re_x^{-1/2}Nu_x)$ number moves towards λ when the parameters of Z are varied. As Z rises, the amount of $(Re_x^{1/2}C_f)$ and $(Re_x^{-1/2}Nu_x)$ will increase in intensity. This illustrates that the inclusion of λ and Z resulted in an increase in the amplitudes of the function $f'(0)$. In addition to this, it was shown that the values of $-\theta'(0)$ increased as the strength of the Lorentz force grew. In addition to this, it has also been observed that the $(Re_x^{1/2}C_f)$ and $(Re_x^{-1/2}Nu_x)$ are higher when there is aggregation present as compared to when there is none present at all.

In Fig. 14 (A), the relationships between the $(Re_x^{1/2}C_f)$ and $(Re_x^{-1/2}Nu_x)$ for the heat source constraint S and λ are sightseen for both situations (without aggregation and with aggregation). Fig. 14 (A) displays the $(Re_x^{-1/2}Nu_x)$ profile, which may be used to get unique estimations of the S . As S is increased, the graph for nanofluids demonstrates that the $(Re_x^{-1/2}Nu_x)$ decreases. More heat added to the nanofluid raises the fluid's temperature, which in turn reduces the efficiency with which heat can be transported according to the laws of physics. Fig. 14(B) displays the influence that the magnetic parameter, M , has on the $(Re_x^{-1/2}Nu_x)$ of nanofluid for both the model without aggregation effects and the model with aggregation effects. Additional observations demonstrate that the increase in M resulted in a marginal decrease in the $(Re_x^{-1/2}Nu_x)$ amounts, as shown in Fig. 14 (B). In this case, it is possible to notice that the presence of M lowered the heat transfer rate owing to the rise in the thickness of the thermal boundary layer, which led to a lower amount of heat flux being created. In a purely physical sense, the frictional force that exists within the fluid flow and the wall of resistance that forms the Lorentz force are responsible for the release of energy. As a result, it is possible that it will contribute to increasing the thickness of the thermal boundary layer by releasing a load of energy as a result of the frictional force. Additionally, the presence of M -induced electrical currents in the fluid may result in a loss of energy and a decrease in the temperature gradient between the fluid and the surface. This, in turn, leads to a reduction in the value of the $(Re_x^{-1/2}Nu_x)$, which in turn results in a decrease in the rate at which heat is transferred. In light of these findings, it would seem that the addition of a magnetic field to the flow of the boundary layer might potentially speed up the process of boundary layer separation while also expanding the number of possible solutions.

Graphs of the $(Re_x^{-1/2}Nu_x)$ toward the λ are shown in Fig. 15(A) for a wide variety of Biot numbers Bi values. These graphs cover a large range of values. Within the plate, the temperature is extremely close to being consistent, and the temperature difference between the fluid border layer and the rest of the plate is also very small. In spite of this, the result that is shown in Fig. 15(A) is evidence that Bi has a primary influence on the rate of heat transfer. This is because the $(Re_x^{-1/2}Nu_x)$ values increase with the ramp-up value of Bi . The Biot number has an inverse relationship with thermal resistance in terms of the physical world since it may be directly related to the heat transfer coefficient, h_f . Because of this, there will be an increase in the rate of surface heat transfer because the heat resistance will go down as Bi rises, as shown in Fig. 15 (A). In addition to this, there was an increase in heat flow since the existence of Bi decreased the thickness of the thermal barrier layer. In addition to that, Fig. 15(B) outlines the Eckert number as well as the effect that Ec has on the $Re_x^{-1/2}Nu_x$ when λ is involved. In its most basic form, the Ec could be understood to represent the potential ratio of advective transport to heat dissipation. In a purely physical sense, the acceleration of the Eckert number may be attributed to the coordinated efforts of the joule heating, the viscosity, and the magnetic field. In addition to this, the results that were given in Fig. 15(B) show that the value of the $Re_x^{-1/2}Nu_x$ falls as the value of Ec grows. On a purely physical level, the production of heat on a conducting moving plate is referred to as "joule heating," and it is caused when an electric current source is sent through the plate in question. In addition, the frictional forces between fluid and particles generate a higher Ec value and generate a larger amount of heat. This indicates that more heat was generated throughout the process, which led to an increase in the thickness of the thermal boundary layer. This, in turn, led to a reduction in convective heat transfer, which in turn led to a lower value for the $Re_x^{-1/2}Nu_x$. As a result, in this circumstance, an increasing Ec value has a tendency to have a negative impact on the efficiency with which heat is transferred.

6. Conclusion

The steady stagnation point of a mixed convection $TiO_2/C_2H_6O_2$ flow that is being accomplished by the application of permeable Riga plates with porous media is the subject of research that is now being conducted. After that, the RK-IV function in MATHEMATICA is used to do a numerical solution on the self-similar equations that were produced as a result of the similarity transformation. For both cases without and with aggregation effects, we analyze in depth the role played by the Eckert number, EMHD parameter, Biot number, porosity parameter, suction parameter, and nanoparticle volume fraction. The following is a list of the most important results from the study:

- The widespread use of aggregation models may be attributed to the fact that they provide more precise velocity and temperature profiles than their homogeneous counterparts.
- Velocity profile rises with cumulative values of ε, K, φ and λ .
- Temperature profile upsurges with growing values of φ, Bi, S, Ec and M , whereas decreases against ε, K and λ .
- The increase in skin friction caused by changing the nanoparticle volume fraction from $\varphi = 0.0$ to $\varphi = 0.01$ for the without aggregation model was about 7.2% for the case of opposing flow area ($\lambda = -1.0$) and 7.5% for the case of aiding flow region ($\lambda = 1.0$).
- With the aggregation model, the heat transfer rate decreases by approximately 3.6% for cases with opposing flow regions ($\lambda = -1.0$) and 3.7% for cases with assisting flow regions ($\lambda = 1.0$), depending on the nanoparticle volume fraction and ranging from $\varphi = 0.0$ to $\varphi = 0.01$, respectively.
- Increases in the value of ε led to significant improvements in the rates of heat transfer and surface friction, which in turn make it easier to bring the boundary layer separation down.
- Because of the energy that is liberated when the force of friction among fluid flows and the resistance exerted by the Lorentz force interacts, the presence of the magnetic parameter M decreased heat transfer performance and augmented the thermal boundary layer thickness.
- An intensification in Ec , which results from joule heating, inhibits the performance of heat transfer, but an upsurge in Bi , has the opposite effect and speeds up the rate of heat transfer in both areas with aiding and opposing flows.

Researchers in fields as diverse as mathematics, mechanics, and physics might benefit from this work since it examines how to control (upsurge or lessening) the heat transfer rate by modifying the characteristics or capabilities of the computer system. All these areas might learn something from this research. The data that has been revealed so far is only relevant to the copper and water combo. To get the same or similar outcome, other scientists may experiment with various conventional nanofluids, hybrid nanofluids, tri-hybrid nanofluids, or other physical properties.

Author contribution statement

Hakeem A. Otman: Analyzed and interpreted the data; Wrote the paper.

Zafar Mahmood, Umar Khan: Conceived and designed the experiments; Contributed reagents, materials, analysis tools or data.

Sayed M Eldin: Performed the experiments; Wrote the paper.

Bandar M. Fadhl: Analyzed and interpreted the data.

Basim M. Makhdoum: Performed the experiments.

Data availability statement

Data will be made available on request.

Declaration of competing interest

The authors declare that they have no known competing financial interests or personal relationships that could have appeared to influence the work reported in this paper

References

- [1] Z. Mahmood, S.E. Alhazmi, A. Alhawaity, R. Marzouki, N. Al-Ansari, U. Khan, MHD mixed convective stagnation point flow of nanofluid past a permeable stretching sheet with nanoparticles aggregation and thermal stratification, *Sci. Rep.* 12 (1) (2022) 1–26.
- [2] N. Ramachandran, T.S. Chen, B.F. Armaly, *Mixed Convection in Stagnation Flows Adjacent to Vertical Surfaces*, 1988.
- [3] J.H. Merkin, Mixed convection boundary layer flow on a vertical surface in a saturated porous medium, *J. Eng. Math.* 14 (4) (1980) 301–313.
- [4] K. Rafique, Z. Mahmood, H. Alqahtani, S.M. Eldin, Various nanoparticle shapes and quadratic velocity impacts on entropy generation and MHD flow over a stretching sheet with joule heating, *Alex. Eng. J.* 71 (2023) 147–159, <https://doi.org/10.1016/j.aej.2023.03.021>.
- [5] S. Choi, J. Eastman, *Enhancing Thermal Conductivity of Fluids with Nanoparticles*, 1995.
- [6] A. Mishra, M. Kumar, Velocity and thermal slip effects on MHD nanofluid flow past a stretching cylinder with viscous dissipation and Joule heating, *SN Appl. Sci.* 2 (8) (2020) 1–13.
- [7] A. Mishra, M. Kumar, Thermal performance of MHD nanofluid flow over a stretching sheet due to viscous dissipation, Joule heating and thermal radiation, *Int. J. Appl. Comput. Math.* 6 (4) (2020) 123.
- [8] A. Mishra, M. Kumar, Numerical analysis of MHD nanofluid flow over a wedge, including effects of viscous dissipation and heat generation/absorption, using Buongiorno model, *Heat Transf* 50 (8) (2021) 8453–8474.

- [9] A. Mishra, H. Upreti, A comparative study of Ag–MgO/water and Fe₃O₄–CoFe₂O₄/EG–water hybrid nanofluid flow over a curved surface with chemical reaction using Buongiorno model, *Partial Differ. Equations Appl. Math.* 5 (2022), 100322.
- [10] S. Akbari, S. Faghiri, P. Poureslami, K. Hosseinzadeh, M.B. Shafii, Analytical solution of non-Fourier heat conduction in a 3-D hollow sphere under time-space varying boundary conditions, *Heliyon* 8 (12) (2022), e12496.
- [11] K. Hosseinzadeh, et al., Investigation of second grade viscoelastic non-Newtonian nanofluid flow on the curve stretching surface in presence of MHD, *Results Eng* 17 (2023), 100838.
- [12] M.M. Gulzar, A. Aslam, M. Waqas, M.A. Javed, K. Hosseinzadeh, A nonlinear mathematical analysis for magneto-hyperbolic-tangent liquid featuring simultaneous aspects of magnetic field, heat source and thermal stratification, *Appl. Nanosci.* 10 (2020) 4513–4518.
- [13] S. Faghiri, S. Akbari, M.B. Shafii, K. Hosseinzadeh, Hydrothermal analysis of non-Newtonian fluid flow (blood) through the circular tube under prescribed non-uniform wall heat flux, *Theor. Appl. Mech. Lett.* 12 (4) (2022), 100360.
- [14] X. Jianhua, D. Liangming, C. Zhou, H. Zhao, J. Huang, T. Sulian, Heat transfer performance and structural optimization of a novel micro-channel heat sink, *Chinese J. Mech. Eng. Ji xie gong cheng xue bao* 35 (1) (2022).
- [15] Z.-Z. Luo, et al., Extraordinary role of Zn in enhancing thermoelectric performance of Ga-doped n-type PbTe, *Energy Environ. Sci.* 15 (1) (2022) 368–375.
- [16] G. Revathi, L.L. Animasau, V.S. Sajja, M. Jayachandra Babu, N. Boora, C.S.K. Raju, Significance of adding titanium dioxide nanoparticles to an existing distilled water conveying aluminum oxide and zinc oxide nanoparticles: scrutinization of chemical reactive ternary-hybrid nanofluid due to bioconvection on a convectively heated surface, *Nonlinear Eng.* 11 (1) (2022) 241–251.
- [17] H.N.C. Dharma, et al., A review of titanium dioxide (TiO₂)-based photocatalyst for oilfield-produced water treatment, *Membranes* 12 (3) (2022) 345.
- [18] R. Giti, M. Firouzmandi, N. Zare Khafri, E. Ansarifard, Influence of different concentrations of titanium dioxide and copper oxide nanoparticles on water sorption and solubility of heat-cured PMMA denture base resin, *Clin. Exp. Dent. Res.* 8 (1) (2022) 287–293.
- [19] P.R. Jubu, K.M. Chahrour, F.K. Yam, O.M. Awoji, Y. Yusof, E.B. Choo, Titanium oxide nanotube film decorated with β-Ga₂O₃ nanoparticles for enhanced water splitting properties, *Sol. Energy* 235 (2022) 152–162.
- [20] A. Fujishima, T.N. Rao, D.A. Tryk, Titanium dioxide photocatalysis, *J. Photochem. Photobiol. C Photochem. Rev.* 1 (1) (2000) 1–21.
- [21] K. P. P. S. R. C. SUS, J.A. Eastman, Mechanisms of heat flow in suspensions of nano-sized particles (nanofluids) *Int. J. Heat Mass Tran.* 45 (4) (2002) 855–863.
- [22] B.-X. Wang, L.-P. Zhou, X.-F. Peng, A fractal model for predicting the effective thermal conductivity of liquid with suspension of nanoparticles, *Int. J. Heat Mass Tran.* 46 (14) (2003) 2665–2672.
- [23] J. Cai, X. Hu, B. Xiao, Y. Zhou, W. Wei, Recent developments on fractal-based approaches to nanofluids and nanoparticle aggregation, *Int. J. Heat Mass Tran.* 105 (2017) 623–637.
- [24] B.M. Makhdom, Z. Mahmood, U. Khan, B.M. Fadhil, I. Khan, S.M. Eldin, Impact of suction with nanoparticles aggregation and joule heating on unsteady MHD stagnation point flow of nanofluids over horizontal cylinder, *Heliyon* 9 (2023).
- [25] B.M. Makhdom, Z. Mahmood, B.M. Fadhil, M.S. Aldhabani, U. Khan, S.M. Eldin, Significance of entropy generation and nanoparticle aggregation on stagnation point flow of nanofluid over stretching sheet with inclined Lorentz force, *Arab. J. Chem.* (2023), 104787, <https://doi.org/10.1016/j.arabjc.2023.104787>.
- [26] K. Guedri, Z. Mahmood, B.M. Fadhil, B.M. Makhdom, S.M. Eldin, U. Khan, Mathematical Analysis of Nonlinear Thermal Radiation and Nanoparticle Aggregation on Unsteady MHD Flow of Micropolar Nanofluid over Shrinking Sheet, *Heliyon*, 2023.
- [27] A. Gailitis, On the possibility to reduce the hydrodynamic drag of a plate in an electrolyte, *Appl. Magneto hydrodyn. Rep. Inst. Phys. Riga* 13 (1961) 143–146.
- [28] S.K. Rawat, A. Mishra, M. Kumar, Numerical study of thermal radiation and suction effects on copper and silver water nanofluids past a vertical Riga plate, *Multidiscip. Model. Mater. Struct.* 15 (2019) 714–736.
- [29] E. Grinberg, On determination of properties of some potential fields, *Appl. Magneto hydrodyn.* 12 (1961) 147–154.
- [30] M. Ayub, T. Abbas, M.M. Bhatti, Inspiration of slip effects on electromagneto hydrodynamics (EMHD) nanofluid flow through a horizontal Riga plate, *Eur. Phys. J. A* 131 (2016) 1–9.
- [31] U. Khan, Z. Mahmood, S.M. Eldin, B.M. Makhdom, B.M. Fadhil, A. Alshehri, Mathematical analysis of heat and mass transfer on unsteady stagnation point flow of Riga plate with binary chemical reaction and thermal radiation effects, *Heliyon* (2023), e14472, <https://doi.org/10.1016/j.heliyon.2023.e14472>.
- [32] S. Goldstein, On backward boundary layers and flow in converging passages, *J. Fluid Mech.* 21 (1) (1965) 33–45.
- [33] A. Mishra, M. Kumar, Influence of viscous dissipation and heat generation/absorption on Ag-water nanofluid flow over a Riga plate with suction, *Int. J. Fluid Mech. Res.* 46 (2) (2019).
- [34] K. Hiemenz, Die Grenzschicht an einem in den gleichförmigen Flüssigkeitsstrom eingetauchten geraden Kreiszyylinder, *Dinglers Polytech. J.* 326 (1911) 321–324.
- [35] F. Homann, Der Einfluss grosser Zähigkeit bei der Strömung um den Zylinder und um die Kugel, *ZAMM-Journal Appl. Math. Mech. für Angew. Math. und Mech.* 16 (3) (1936) 153–164.
- [36] C.Y. Wang, Stagnation flow towards a shrinking sheet, *Int. J. Non Lin. Mech.* 43 (5) (2008) 377–382.
- [37] S. Ahmad, I. Pop, Mixed convection boundary layer flow from a vertical flat plate embedded in a porous medium filled with nanofluids, *Int. Commun. Heat Mass Tran.* 37 (8) (2010) 987–991.
- [38] M. Sheikholeslami, Z. Ziaabakhsh, D.D. Ganji, Transport of Magneto hydrodynamic nanofluid in a porous media, *Colloids Surfaces A Physicochem. Eng. Asp.* 520 (2017) 201–212.
- [39] S. Abu Bakar, N.M. Arifin, F. Md Ali, N. Bachok, R. Nazar, I. Pop, A stability analysis on mixed convection boundary layer flow along a permeable vertical cylinder in a porous medium filled with a nanofluid and thermal radiation, *Appl. Sci.* 8 (4) (2018) 483.
- [40] P. Rana, R. Bhargava, Numerical study of heat transfer enhancement in mixed convection flow along a vertical plate with heat source/sink utilizing nanofluids, *Commun. Nonlinear Sci. Numer. Simul.* 16 (11) (2011) 4318–4334.
- [41] D. Pal, G. Mandal, K. Vajravalu, Mixed convection stagnation-point flow of nanofluids over a stretching/shrinking sheet in a porous medium with internal heat generation/absorption, *Commun. Numer. Anal.* 2015 (2015) 30–50.
- [42] N.S. Khashi'ie, N. Md Arifin, I. Pop, Mixed convective stagnation point flow towards a vertical Riga plate in hybrid Cu-Al₂O₃/water nanofluid, *Mathematics* 8 (6) (2020) 912.